HOT WIRE AND SPARK PYROLYSIS AS SIMPLE NEW ROUTES TO SILICON NANOPARTICLE SYNTHESIS

M. R. Scriba[1], D.T. Britton[2] and M. Härting[2]
[1] National Centre for Nano-Structured Materials, CSIR, P O Box 395, Pretoria 0001, South Africa.
[2] Dept. of Physics, University of Cape Town, Rondebosch 7701, South Africa.

ABSTRACT

Monocrystalline silicon nanoparticles with a mean diameter of between 30 and 40 nm have been synthesised by hot wire thermal catalytic and spark pyrolysis at a pressure of 40 and 80 mbar respectively. For the production a mixture of the precursor gases, silane and diborane or silane and phosphine were used. While hot wire pyrolysis always results in multifaceted particles, those produced by spark pyrolysis are spherical. Electrical resistance measurements of compressed powders showed that boron doped silicon powders have a much higher conductivity than those doped with phosphorus. TEM and XPS analysis reveals that the difference in electrical resistivity between boron an phosphorus doped particles can be attributed to phosphorus dopants being located at the surface of the particles where an oxide layer is also observed. In contrast, boron doped particles are far less oxidised and the dopant atoms can be found in the core of the particle. The results demonstrate that hot wire and spark pyrolysis offer a new simple route to the production of monocrystalline doped silicon nanoparticles suitable for printed electrical devices.

INTRODUCTION

Silicon can be considered the semiconductor with the most useful properties for the manufacture of electronic devices such as individual transistors, integrated circuits and solar cells. However, due to the nature of the devices and their manufacturing processes, applications are generally limited to rigid mounting without the option of flexibility. Recently, printed electronics, based on silicon nanoparticle inks[1], has emerged as a new route to electrical device production. The technology currently allows the printing of silicon based devices on flexible media such as paper and polymers[2]. In these applications the printed nanoparticle network must be able to act as an extrinsic semiconductor, thus requiring the silicon nanoparticles to be doped and free of an oxide layer. Current bottom-up production processes for silicon nanoparticles include chemical vapour synthesis by laser or plasma pyrolysis[3] and laser ablation[4] at low pressure (high vacuum). In an attempt to find new simple routes for the synthesis of silicon nanoparticles , hot wire thermal catalytic pyrolysis (HWTCP)[5, 6] and spark pyrolysis (SP) have been applied. Whereas HWTCP is based on the well known technique of hot wire chemical vapour deposition, spark pyrolysis has been utilized for the first time in the production of silicon nanoparticles. In this process the spark can be defined as a sudden breakdown or ionisation of the precursor gas or vapour, due to a high electric field between two electrodes. Free electrons and to a lesser extent ions, form the current of charge carriers in the plasma of the spark[7] resulting in a near instantaneous heat source[8] reaching temperatures between 5000 °C and 22000 °C[9] in a few micro seconds. This high temperature heat source rapidly dissociates the silane and dopant gases during the production of doped silicon nanoparticles. Although electrically excited, spark pyrolysis has the most similarities with pulsed laser pyrolysis of precursor gases, which also has short heating and rapid cooling cycles[10].

EXPERIMENTAL

A basic vacuum system, in which the pressure, precursor gas flow rate and either the filament temperature or spark gap can be changed, was constructed to accommodate both HWTCP and SP configurations. Two sets of nanopowders were produced by each method, at a precursor flow rate of 50 sccm, firstly with a mixture of diborane (B_2H_6) and silane (SiH_4) and secondly with a mixture of phosphine (PH_3) and silane. Dopant gases were administered at ratios of 0.01, 0.1 and 1%. The

production pressure for SP was 80 mbar and that of HWTCP 40 mbar. For all HWTCP synthesis experiments the filament temperature was maintained at 1800ºC. For SP synthesis the spark was generated by continuously charging and discharging the high voltage power supply capacitor in a free running mode yielding an approximate energy of 0.6 J at a frequency of about 10 Hz. This frequency is determined by the breakdown voltage and power supply characteristics. Each production run of up to 20 minutes resulted in a layer of ochre to brown powder covering all internal surfaces of the reaction chamber. The powder was harvested after opening to air and stored in glass bottles without any special treatment.

The bulk crystallinity of the powders was investigated by x-ray powder diffraction (XRD), performed with a Panalytical PW3040/60 E'Pert Pro diffractometer, operated with CuKα radiation with a wavelength of 0.15406 nm. A JEOL JSM7500F analytical Field Emission scanning electron microscope (SEM) and a Thermo Scientific UltraDry silicon drift detector were used to collect energy dispersive x-ray spectroscopy (EDX) spectra at 5 keV, and the internal structure of the silicon nanoparticles was investigated using a JEOL 2100 TEM at 200kV acceleration voltage. A Physical Electronics Quantum 2000 x-ray photoelectron spectroscopy (XPS) system with monochromatic Al Kα radiation was used to investigate the surface composition of the nanoparticles. Lastly, the electrical characteristics of nanopowders were determined using a system specifically constructed for that purpose. For each sample, about 20 mg of powder was loaded into a plastic cylinder of 8.85 mm internal diameter and compressed between two stainless steel rods which also serve as the electrical contacts. The applied force was set with a calibrated load cell to 2.55 MPa and the change in separation of the pistons was measured by a micrometer. Current—voltage (I-V) curves were measured in current sweeping mode using a Keithley 4200 semiconductor characterisation system at room temperature (23°C). A similar electrical characterisation approach has been used by other groups on lead dioxide powders [11] and metal powders [12]. The conductivity of the compacted powders was determined from the measured resistance by

$$\sigma = \frac{h}{RA}, \qquad (1)$$

where h is the distance between the contacts, R the resistance, and A the cross sectional area of the compressed powder.

RESULTS

From the narrow, well defined peaks in the X-ray powder diffraction patterns of the silicon nanoparticles shown in figure 1, which do not show any contribution from an amorphous phase, the crystalline nature of all powders, is evident. The sharp peaks at 28.5°, 47° and 56° correspond to the (111), (220) and (311) crystal planes of crystalline silicon, and the three higher order peaks at 69° (400), 76.5° (331) and 88° (422) are also clearly visible.

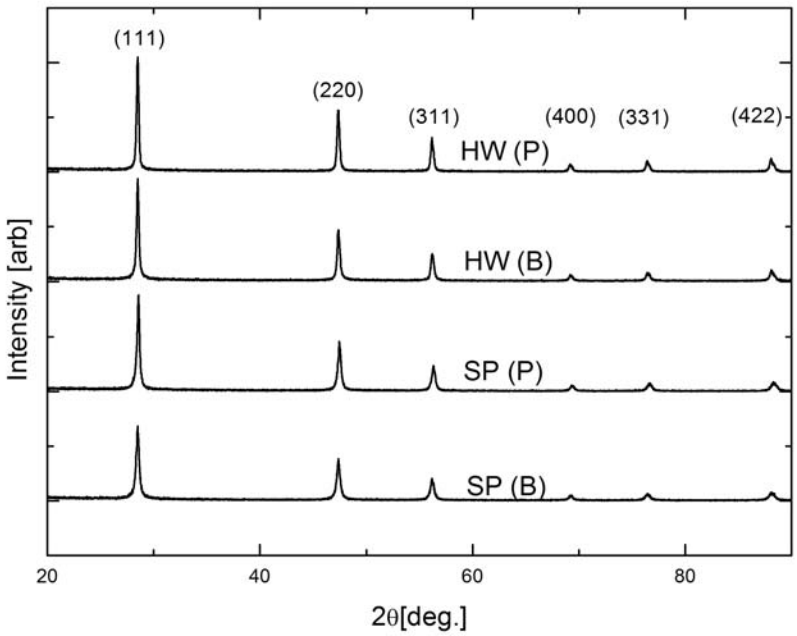

Figure 1. XRD patterns of silicon nanopowders produced with 1% dopant gas concentration by HWTCP (marked HW) and SP with diborane (marked B) and phosphine (marked P).

TEM studies clearly show that the nanoparticles are all monocrystalline irrespective of the production method or dopant gas. However, the TEM images reveal that HWTCP particles are always multifaceted (Fig 2a) and those produced by SP are always spherical (Fig 2b).

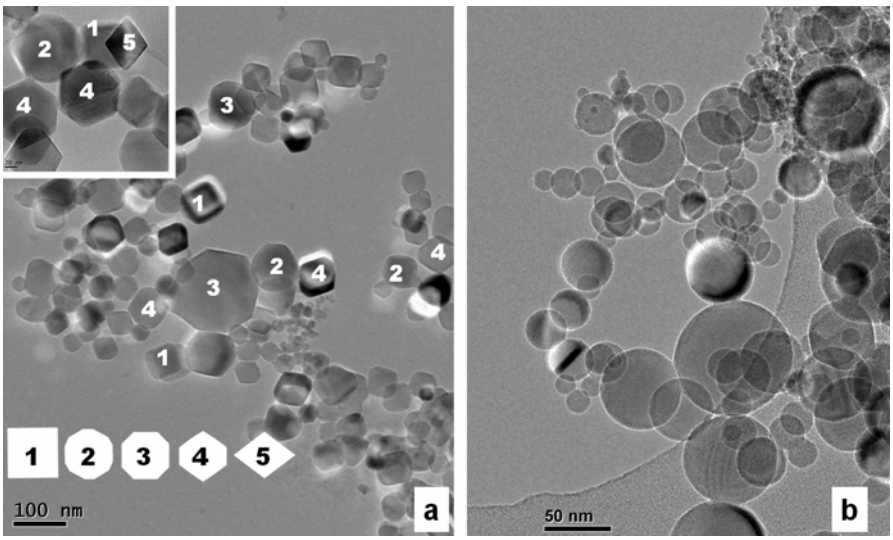

Figure 2. Example of silicon nanoparticles produced by (a) HWTCP (multifaceted) and (b) TCP (spherical). The numbered insets represent different projected views of the same basic morphology with a shape ranging from an octahedron to a truncated octahedron[13].

The mean diameter of all particles irrespective of the production method, pressure or dopant gas concentration is below 50 nm, however a small fraction of nanoparticles with diameters up to 150 nm is also present in these powders. At a higher TEM magnification a thin outer layer of a general amorphous nature on particles produced with phosphine (figure 3a) is revealed. From the TEM studies it was found that the thickness of this outer layer on the nanoparticles may be up to the equivalent of 3 of the (111) crystal planes, or about 0.6 nm, in the silicon nanoparticles produced at the highest dopant levels. Particles produced with diborane generally have lattice planes that extend to the surface (figure 3b) indicating the absence of disorder (amorphous shell).

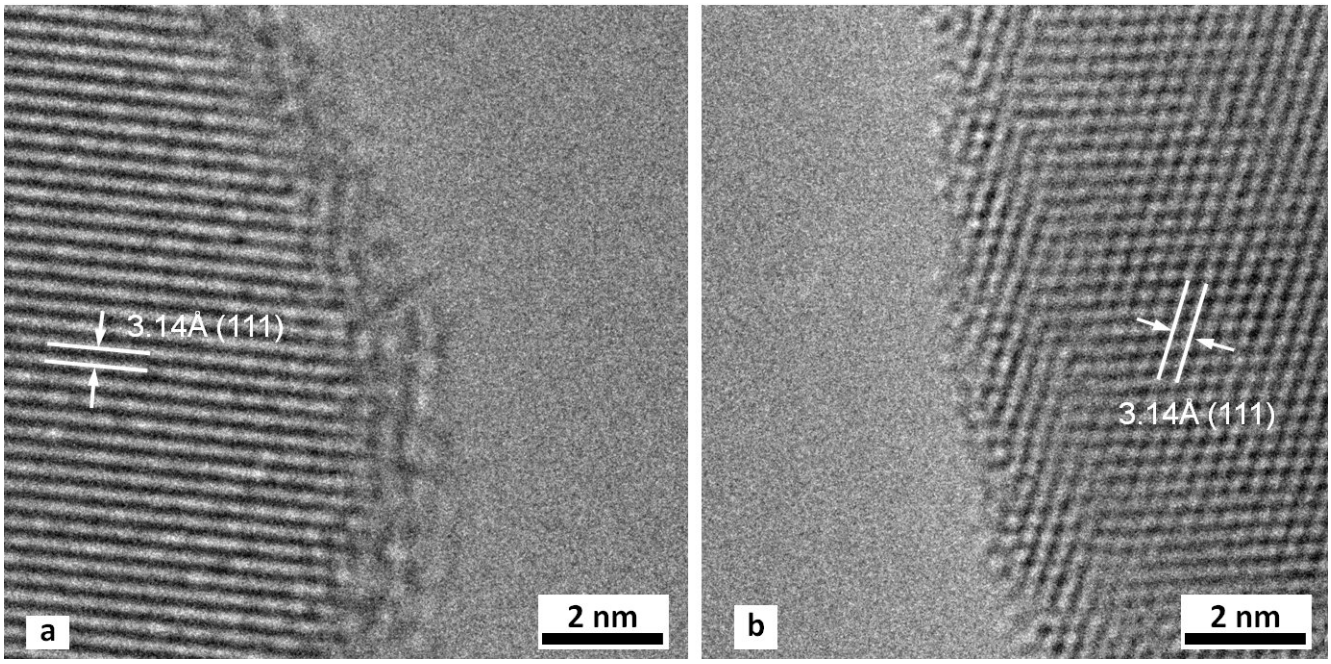

Figure 3. Surface structure of nanoparticles produced by SP with (a) 0.01% phosphine, and (b) 0.1% diborane. In both images the (111) crystal orientation is indicated.

Furthermore, by studying TEM images of all particles, it was observed that the amorphous surface region generally increases in thickness with an increase in dopant gas concentration for both phosphorus and boron doped silicon nanoparticles. The general composition of the powders was determined by EDX, and as shown by the inset example in figure 4, the particles comprise mainly silicon and oxygen with a small percentage of the dopant.

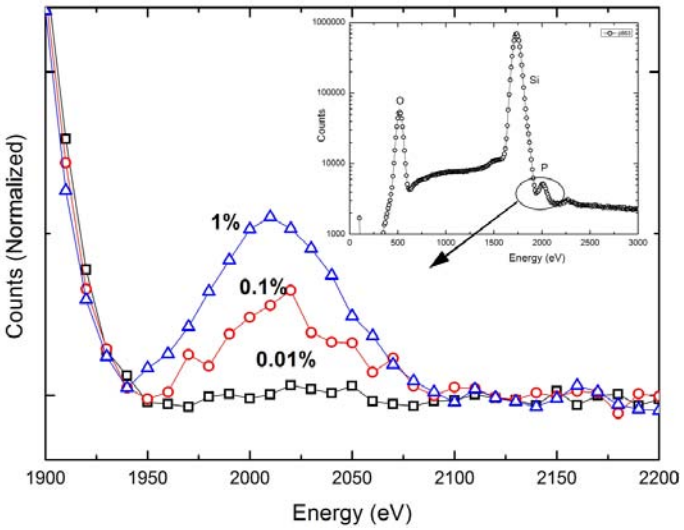

Figure 4. EDX spectra of particles produced by SP at 80 mbar showing an increase of phosphorus in the powder for an increase in phosphine concentration (from 0.01% to 0.1% and 1%) during production.

The increase in the intensity of the phosphorus peak (at about 2020 eV) shown in figure 4 indicates an increase in phosphorus atoms present in the particles with an increase in phosphine concentration during production (from 0.01 to 1%). The surface region of the nanoparticles was further investigated by XPS. Of special interest is the determination of the silicon oxide. For this reason, the silicon 2p peaks in the XPS spectrum at around 100 eV were analysed, after subtracting the background of the spectra, using the iterative Shirley method[14]. This region of the spectrum contains information on all silicon oxidation states. The contribution of the silicon sub-oxides was now determined by achieving a best least squares fit (Figure 5) from fitting for all 5 peaks corresponding to the different oxidation states of silicon[15].

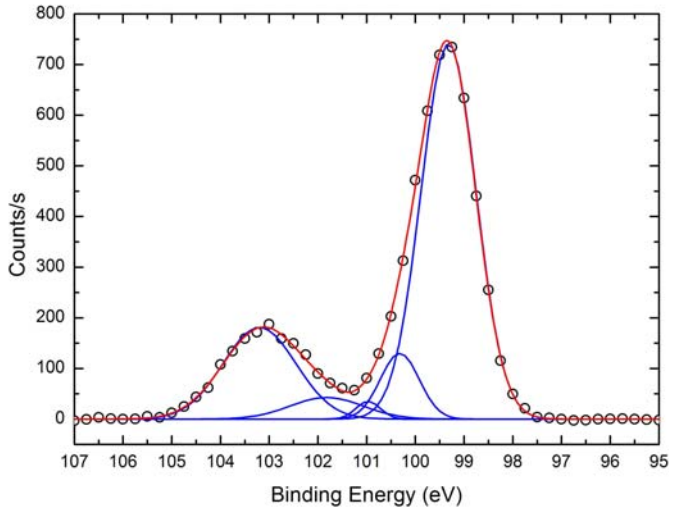

Figure 5. An example XPS spectrum of silicon nanoparticles showing the best least squares fit achieved, with 5 Gaussian peaks at about: 99.0 eV (Si), 100.0 eV (Si^{1+}), 100.65 eV (Si^{2+}), 101.5 eV (Si^{3+}), 103.0 eV (Si^{4+}).

To estimate the shell thickness on the silicon nanoparticles attributable to SiO_2, the ratio of the integrated intensities of the XPS peaks corresponding to Si and SiO_2 was used. For Si 2p photoelectrons the perpendicular escape depth in silicon is 2.11 nm. Using a maximum escape depth of 3.80 nm[16], an approximate depth of 1.9 nm in SiO_2 and 1.055 nm in silicon is probed by the XPS measurement. These values were used to calculate the average thickness of the SiO_2 layer for all particles, using the equation:

$$y = \frac{P_{SiO_2} \times R_X}{(R_X + 1)} \qquad (2)$$

where y is the thickness of the SiO_2 layer, P_{SiO2} is the photoelectron escape depth in SiO_2 and R_X is the ratio of the integrated intensities of the SiO_2 and silicon photoemission peaks. Using this method the estimated SiO_2 layer thicknesses for the silicon powders were determined and are presented in figure 6.

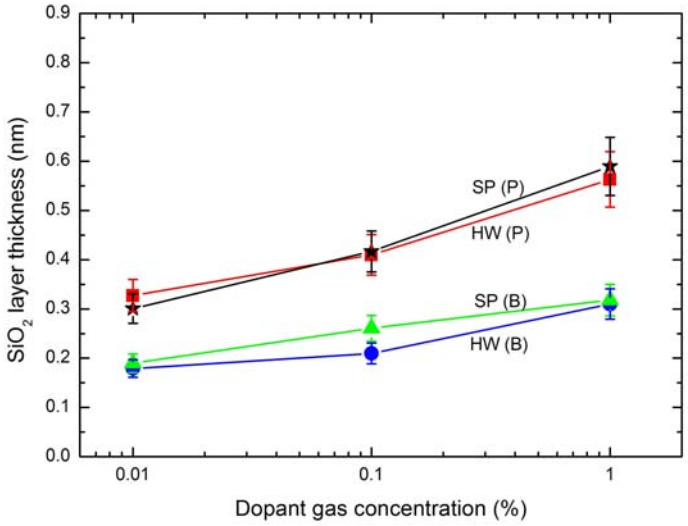

Figure 6. The estimated SiO_2 layer thickness of all particles at different dopant gas concentrations.

The results confirm the TEM observations: for particles produced with high phosphorus doping levels the fully oxidised silicon layer is up to 0.6 nm thick. Furthermore the SiO_2 content in the surface region of all nanoparticles produced in the presence of both dopant gases increases with increasing dopant concentration. The SiO_2 content in phosphorus doped particles is twice that of particles produced with boron as dopant. To determine the concentration of dopant atoms in the surface region of the doped silicon nanoparticles the boron 1s photoemission peak at about 188 eV[17] as well as the phosphorus P-O peak at 135 eV [18-20] and the combined P 2p peak, at 131 eV [20-23] were analysed. The ratio of the intensities of the boron peak and as the P-O bond, to the SiO_2 of all powders are shown in figure 7(a) and 7(b) respectively.

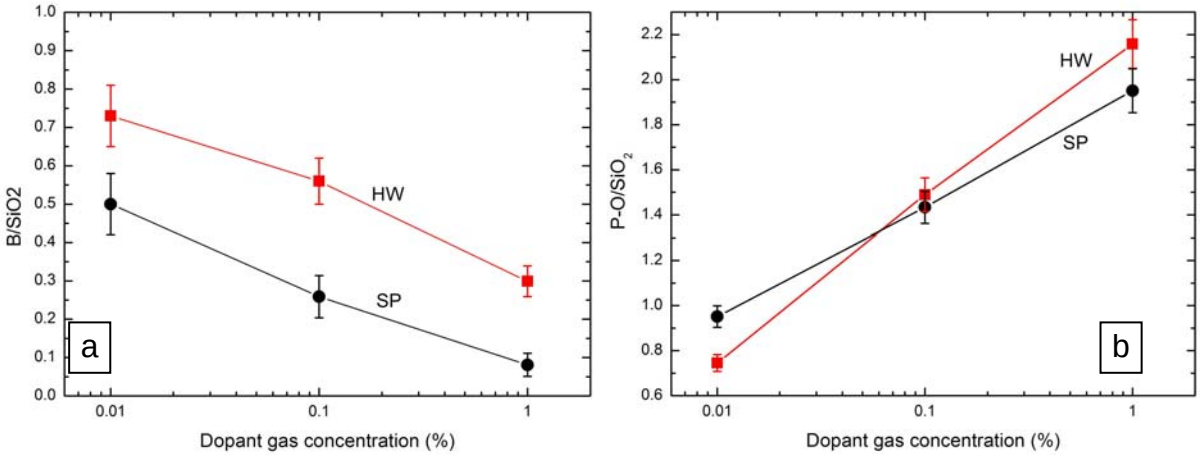

Figure 7. Comparison of dopant concentrations as a ratio of SiO_2 in all silicon nanopowders produced with (a) diborane (b) phosphine.

With an increase in dopant gas concentration, the number of dopant atoms in the outer 2-3 nm (max XPS probe depth) of nanoparticles decreases in the case of boron (figure 7a) and increases in the case of phosphorus (figure 7b). This observation is made for powders of both production methods.

Finally, the resistivity of all silicon nano-powders was measured using the method described earlier.

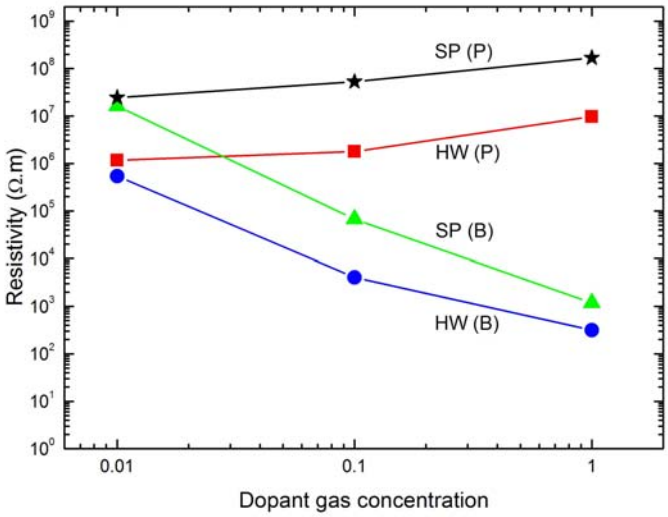

Figure 8. A comparison of the resistivity values of all powders produced by HWTCP and SP with varying concentrations of phosphine and diborane.

The resistivity curves shown in figure 8 reveal that powders produced by HWTCP and SP with diborane (marked as HW (B) and SP (B)) exhibit a decrease in resistivity with an increase in diborane concentration. In contrast, powders produced with phosphine (marked as HW (P) and SP (P)) show an increase in resistivity with an increase in phosphine concentration. Furthermore all powders produced by SP show a higher resistivity compared to powders produced by HWTCP, at the equivalent dopant concentrations.

DISCUSSION

Since the silicon nanoparticles produced in this study are ultimately intended for applications in printed electronic devices, the electrical characteristics of the powders are important. Furthermore, the resistivity will depend primarily on the composition of the particles, their doping concentration, the packing density (compression)[24], as well as the presence and thickness of an oxide layer on the surface of particles.

While particles produced with boron exhibit electrical activity those produced with phosphorus show an increase in resistivity with an increase in phosphine concentration. EDX analysis has indicated that this increase cannot be ascribed to the failure to incorporate phosphorous (fig 4) but rather to the increase in the thickness of a stoichiometric oxide layer on the surface of these particles (figure 6) with an increase in dopant gas concentrations. Furthermore, the phosphorous atoms are located near the particle surface. This is apparent from the substantial increase in P-O bonds (figure 7b) with the increase in the oxide layer thickness of these particles. In particles doped with boron, the maximum stoichiometric oxide detected at high dopant levels is below 0.3 nm (figure 6) and thus cannot be considered an oxide layer. Nevertheless, an increase in SiO_2 content with increased diborane gas levels is detected and corresponds to a decrease in the boron content in the surface region of these particles (figure 7a), indicating that the boron atoms are located inside the nanoparticles. The availability of charge carriers due to this successful doping is thus responsible for the decrease in resistivity with increasing doping levels.

The Cabrera-Mott mechanism [25] offers a possible way of interpreting the thicker oxide layer observed on particles produced with phosphine. A virgin silicon surface on a silicon nanoparticle will rapidly form a thin native oxide layer when exposed to air. Electrons may now tunnel through the thin oxide layer to the surface. Some oxygen atoms adsorbed on the surface will be ionized and acquire a negative charge, to form an electric potential V_{OL} across the oxide layer. Assisted by V_{OL}, oxygen ions diffuse through the silicon oxide layer to oxidise the silicon underneath [3]. From the model it can be deduced that in the case of phosphorous doped silicon nanoparticles there is a higher concentration of free electrons, induced by the phosphorus, especially if the phosphorus is primarily located at the surface. This results in an increase in V_{OL}, which boosts the transport of the oxygen ions through the silicon oxide layer, resulting in a more efficient oxidation. In boron doping, the low electron concentration reduces V_{OL}, and thus boron doped nanoparticles are less efficiently oxidised [3].

The difference in shape between silicon nanoparticles produced by HWTCP and SP is directly linked to their respective synthesis temperatures and cooling rates While the short, high temperature spark creates the conditions for rapid pyrolysis and rapid cooling of nanoparticles, the HWTCP process is characterised by gradual cooling. Both processes are graphically depicted in figure 9. Particles start to form in the supersaturated vapour, by homogeneous nucleation to form liquid silicon droplets [26, 27]. To maintain a minimum surface energy, the droplets are expected to be spherical at this stage. As the pressure in both processes is high, sufficient precursor species collide with the nucleating particles, resulting in accelerated growth. The difference in the shape of particles produced by SP and HWTCP originates from the difference in the rate of cooling, between the processes.

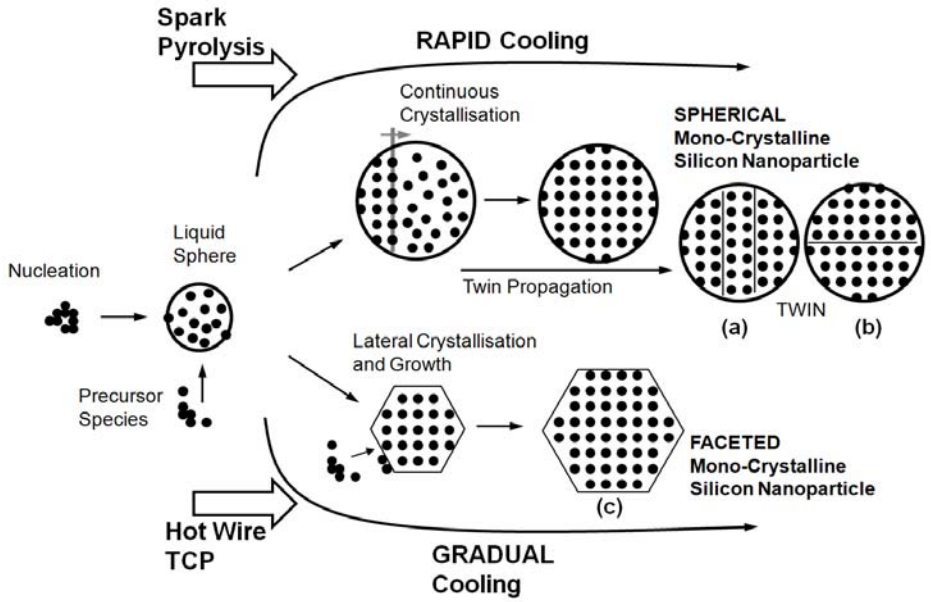

Figure 9 Silicon nanoparticle growth process for spherical and faceted particles.

The high temperature spark, which lasts for approximately 100 ns, creates the conditions for rapid pyrolysis and rapid cooling. Crystallisation of the spherical droplets start from a crystal nucleation site on its edge and propagates through the crystal as a crystallisation front [26] at the solid/liquid interface. The process results in spherical single crystal silicon nanoparticles. Similar results have been reported for laser pyrolysis [27, 28] and plasma synthesis with accelerated cooling [26, 29].

Continuing with figure 9, in contrast to spark pyrolysis, the HWTCP process has a continuous heat source, resulting in continuous pyrolysis and a moderate temperature gradient around the filament. The relatively slow growth rate allows the liquid silicon droplets to gradually cool as they move away from the filament. There is sufficient time and energy for atoms to find energy favourable growth sites. The crystal planes of the nanocrystals therefore start to grow laterally [30] to form faceted particles [31]. Furthermore, species in the vapour have enough energy to find an energy favourable sight and contribute to continued particle growth. Given ideal conditions an individual particle takes the shape with the lowest total surface energy, a truncated octahedron [13, 32-35]. However, the temperature gradient around the filament creates differences in cooling gradients, which is responsible for the different states of faceted shapes in particles produced by HWTCP as shown in figure 2(a).

CONCLUSION

Monocrystalline doped silicon nanoparticles have been produced by hot wire thermal catalytic pyrolysis and spark pyrolysis. The silicon nanoparticles are spherical when synthesised by SP and faceted for HWTCP. While the successful boron doping of the nanoparticles is evident from the decrease in resistivity with increasing dopant concentrations, the same does not apply to silicon nanoparticles doped with phosphorous. The resistivity of phosphorus doped nanoparticles increases with increasing phosphine concentration in the precursor gas. This effect is attributed to the formation of a silicon oxide on the surface of these particles up to a thickness of 0.6 nm. Furthermore, the

phosphorus atoms are not incorporated in the core of the silicon nanoparticle but rather at the interface to the oxide layer where they are electrically inactive. The shape of the nanoparticles is governed by the synthesis temperature and cooling rate of the processes. The short-lived, high temperature and cyclic spark process creates the conditions for rapid pyrolysis and rapid cooling, resulting in spherical particles. In contrast the HWTCP process which has a gradual cooling profile results in the ordered growth of faceted nanoparticles.

ACKNOWLEGEMENT

The authors would like to acknowledge the project financial support of CSIR and the use of the Characterisation Facility at the DST/CSIR National Centre for Nano-Structured Materials, as well as the use of facilities at the University of Cape Town. XPS measurements were performed by W Jordaan at the National Metrology Institute of South Africa.

REFERENCES

[1]D.T. Britton and M. Härting, Printed Nanoparticulate Composites for Silicon Thick Film Electronics, *Pure and Applied Chemistry*, **78**(1723 (2006).

[2]M. Härting, J. Zhang, D.R. Gamota and D.T. Britton, Fully printed silicon field effect transistors, *Applied Physics Letters*, **94**(19), 193509-3 (2009).

[3]X.D. Pi, R. Gresback, R.W. Liptak, S.A. Campbell, and U. Kortshagen, Doping efficiency, dopant location, and oxidation of Si nanocrystals, *Applied Physics Letters*, **92**(12), 123102-3 (2008).

[4]F.E. Kruis, H. Fissan and A. Peled, Synthesis of nanoparticles in the gas phase for electronic, optical and magnetic applications--a review, *Journal of Aerosol Science*, **29**(5-6), 511-535 (1998).

[5]M.R. Scriba, C. Arendse, M. Härting and D.T. Britton, Hot-wire synthesis of Si nanoparticles, *Thin Solid Films*, **516**(5), 844-846 (2008).

[6]M.R. Scriba, D.T. Britton, C. Arendse, M.J. van Staden, and M. Härting, Composition and crystallinity of silicon nanoparticles synthesised by hot wire thermal catalytic pyrolysis at different pressures, *Thin Solid Films*, **517**(12), 3484-3487 (2009).

[7]N. Tabrizi, M. Ullmann, V. Vons, U. Lafont, and A. Schmidt-Ott, Generation of nanoparticles by spark discharge, *Journal of Nanoparticle Research*, (2008).

[8]Z.I. Ashurly, V.V. Gal and V.P. Malin, Temperature field in a pulsed discharge, *Journal of Engineering Physics and Thermophysics*, **20**(1), 45-49 (1971).

[9]R. Ono, M. Nifuku, S. Fujiwara, S. Horiguchi, and T. Oda, Minimum ignition energy of hydrogen-air mixture: Effects of humidity and spark duration, *Journal of Electrostatics*, **65**(2), 87-93 (2007).

[10]H. Hofmeister, P. Kodderitzsch and J. Dutta, Structure of nanometersized silicon particles prepared by various gas phase processes, *Journal of Non-Crystalline Solids*, **232-234**(182-187 (1998).

[11]H. Braun, K.J. Euler and P. Herger, Electronic conductivity of lead dioxide powder: separation of core and surface resistance of the particles, *Journal of Applied Electrochemistry*, **10**(4), 441-448 (1980).

[12]Y.P. Mamunya, H. Zois, L. Apekis and E.V. Lebedev, Influence of pressure on the electrical conductivity of metal powders used as fillers in polymer composites, *Powder Technology*, **140**(1-2), 49-55 (2004).

[13]S. Onaka, Geometrical analysis of near polyhedral shapes with round edges in small crystalline particles or precipitates, *Journal of Materials Science*, **43**(8), 2680-2685 (2008).

[14]J.E. Castle, H. Chapman-Kpodo, A. Proctor and A.M. Salvi, Curve-fitting in XPS using extrinsic and intrinsic background structure, *Journal of Electron Spectroscopy and Related Phenomena*, **106**(1), 65-80 (2000).

[15]M. Niwano, H. Katakura, Y. Takeda, Y. Takakuwa, N. Miyamoto, A. Hiraiwa, and K. Yagi, Photoemission study of the SiO[sub 2]/Si interface structure of thin oxide films on Si(100), (111), and (110) surfaces, *Journal of Vacuum Science and Technology A: Vacuum, Surfaces, and Films*, **9**(2), 195-200 (1991).
[16]K. Hirose, H. Nohira, K. Azuma and T. Hattori, Photoelectron spectroscopy studies of SiO2/Si interfaces, *Progress in Surface Science*, **82**(1), 3-54 (2007).
[17]X.J. Hao, E.C. Cho, C. Flynn, Y.S. Shen, S.C. Park, G. Conibeer, and M.A. Green, Synthesis and characterization of boron-doped Si quantum dots for all-Si quantum dot tandem solar cells, *Solar Energy Materials and Solar Cells*, **93**(2), 273-279 (2009).
[18]Y. Sano, W.B. Ying, Y. Kamiura and Y. Mizokawa, Annealing induced phosphorus protrusion into thin-oxide films from heavily phosphorus-doped silicon (100), *Thin Solid Films*, **516**(8), 1788-1795 (2008).
[19]W.B. Ying, Y. Mizokawa, K. Tanahashi, Y. Kamiura, M. Iida, K. Kawamoto, and W.Y. Yang, Evaluation of the initial oxidation of heavily phosphorus doped silicon surfaces using angle-dependent X-ray photoelectron spectroscopy, *Thin Solid Films*, **343-344**(393-396 (1999).
[20]Y. Mizokawa, W.B. Ying, Y.B. Yu, Y. Kamiura, M. Iida, and K. Kawamoto, Phosphorus redistribution in the surface region of heavily phosphorus doped silicon, *Applied Surface Science*, **100-101**(561-565 (1996).
[21]A.I. Kovalev, D.L. Wainstein, D.I. Tetelbaum, W. Hornig, and Y.N. Kucherehko, Investigation of the electronic structure of the phosphorus-doped Si and SiO_2:Si quantum dots by XPS and HREELS methods., *Surface and Interface Analysis*, **36**(8), 959-962 (2004).
[22]S.F. Yoon and R. Ji, Application of electron cyclotron resonance chemical vapour deposition in the preparation of hydrogenated SiC films: a comparison of phosphorus and boron doping, *Journal of Alloys and Compounds*, **261**(1-2), 281-288 (1997).
[23]X.J. Hao, E.C. Cho, G. Scardera, E. Bellet-Amalric, D. Bellet, Y.S. Shen, S. Huang, Y.D. Huang, G. Conibeer, and M.A. Green, Effects of phosphorus doping on structural and optical properties of silicon nanocrystals in a SiO2 matrix, *Thin Solid Films*, **517**(19), 5646-5652 (2009).
[24]A. Celzard, J.F. Marêché, F. Payot and G. Furdin, Electrical conductivity of carbonaceous powders, *Carbon*, **40**(15), 2801-2815 (2002).
[25]N. Cabrera and N.F. Mott, Theory of the Oxidisation of Metals., *Pep. Prog. Phys.*, **12**(163), (1948).
[26]C.R. Perrey and C.B. Carter, Insights into nanoparticle formation mechanisms, *Journal of Materials Science*, **41**(9), 2711-2722 (2006).
[27]F. Huisken, H. Hofmeister, B. Kohn, M.A. Laguna, and V. Paillard, Laser production and deposition of light-emitting silicon nanoparticles, *Applied Surface Science*, **154-155**(305-313 (2000).
[28]E. Borsella, M. Falconieri, S. Botti, S. Martelli, F. Bignoli, L. Costa, S. Grandi, L. Sangaletti, B. Allieri, and L. Depero, Optical and morphological characterization of Si nanocrystals/silica composites prepared by sol-gel processing, *Materials Science and Engineering B*, **79**(1), 55-62 (2001).
[29]B. Giesen, H. Wiggers, A. Kowalik and P. Roth*, Formation of Si-nanoparticles in a microwave reactor: Comparison between experiments and modelling, *Journal of Nanoparticle Research*, **7**(1), 29-41 (2005).
[30]A. Babat, C. Anderson, C.R. Perry, C.B. Carter, S.A. Campbell, and U. Kortshagen, Plasma synthesis of single-crystal silicon nanoparticles for novel electronic device applications, *Plasma Phys. Control. Fusion*, **46**(B97-B109 (2004).
[31]U.R. Kortshagen, L. Mangolini and A. Babat, Plasma synthesis of semiconductor nanocrystals for nanoelectronics and luminescence applications., *Journal of Nanoparticle Research*, **9**(39-52 (2007).
[32]A.S. Barnard and P. Zapol, A model for the phase stability of arbitrary nanoparticles as a function of size and shape, *The Journal of Chemical Physics*, **121**(9), 4276-4283 (2004).

[33]S. Onaka, A simple equation giving shapes between a circle and a regular N -sided polygon, *Philosophical Magazine Letters*, **85**(7), 359-365 (2005).
[34]K. Kimoto, Morphology and crystal structure of fine particles produced by a gas evaporation technique, *Thin Solid Films*, **32**(2), 363-365 (1976).
[35]Z.L. Wang and J.S. Yin, Self-assembly of shape-controlled nanocrystals and their in-situ thermodynamic properties, *Materials Science and Engineering A*, **286**(1), 39-47 (2000).